

# 1D to 3D Crossover of a Spin-Imbalanced Fermi Gas

Melissa C. Revelle, Jacob A. Fry, Ben A. Olsen,\* and Randall G. Hulet

*Department of Physics & Astronomy and Rice Center for Quantum Materials, Rice University, Houston, TX 77005, USA*

(Dated: May 18, 2022)

We have characterized the one-dimensional (1D) to three-dimensional (3D) crossover of a two-component spin-imbalanced Fermi gas of  ${}^6\text{Li}$  atoms in a 2D optical lattice by varying the lattice tunneling and the interactions. The gas phase separates, and we detect the phase boundaries using *in situ* imaging of the inhomogeneous density profiles. The locations of the phases are inverted in 1D as compared to 3D, thus providing a clear signature of the crossover. By scaling the tunneling rate  $t$  with respect to the pair binding energy  $\epsilon_B$ , we observe a collapse of the data to a universal crossover point at a scaled tunneling value of  $t/\epsilon_B = 0.016(1)$ .

PACS numbers: 67.85.Lm, 71.10.Pm, 37.10.Jk, 05.70.Fh

Spin-imbalanced atomic Fermi gases have been studied extensively in recent years, motivated by a search for exotic superfluid phases [1–3]. One such superfluid, the Fulde-Ferrel-Larkin-Ovchinnikov (FFLO) phase [4, 5], has not been seen in three dimensions (3D) but is believed to occupy a large portion of the one-dimensional (1D) phase diagram [6, 7]. Measurements have confirmed that the 1D phase diagram is consistent with theories exhibiting FFLO [8], but no direct evidence for this phase has been obtained. The FFLO phase is expected to be more robust to quantum fluctuations in higher dimensions, however, thus focusing attention on the dimensional crossover [9–12].

Spin-imbalanced trapped Fermi gases have been observed to phase separate in both 3D [13–15] and in 1D [8]. The nature of this phase separation, is qualitatively different in 3D than in 1D, as shown schematically in Fig. 1(a). In 3D, phase separation of an interacting two-component spin-imbalanced Fermi gas results in a balanced superfluid  $\text{SF}_0$  core surrounded by polarized shells, while in 1D, the core is partially polarized. A crossover between the 1D and 3D regimes may be realized by varying the aspect ratio of the confining potential [16–20]. Although, a complementary dimensional crossover may be achieved by varying the tunneling  $t$  between neighboring tubes aligned in an array, as depicted in Fig. 1(b). Such a geometry, which may be realized with an optical lattice is more analogous to some material systems, such as carbon nanotube bundles [21] and spin-1/2 magnet chains [22, 23]. The bundle will cross over from an array of independent 1D tubes for small  $t$ , to a 3D gas as  $t$  is increased [24, 25]. We have employed this geometry to determine the crossover value of  $t$  for various interaction strengths and find a striking universality in the crossover location.

As described in detail previously [8, 13], our ex-

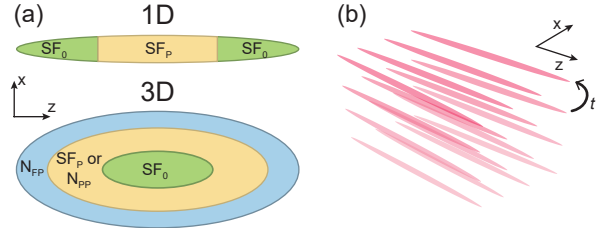


FIG. 1. (Color online) (a) Schematic of phase separation of a spin-imbalanced Fermi gas in 1D (top) and in 3D (bottom) at zero temperature. For 1D, the central region is an LO-type partially polarized superfluid ( $\text{SF}_P$ ), while the wings are either a balanced superfluid ( $\text{SF}_0$ ) for small central tube polarization  $P_t$ , or a fully polarized normal phase ( $\text{N}_{\text{FP}}$ ) (not shown) for  $P_t$  above a critical value  $P_c^{1D}$ . Below a critical polarization in 3D,  $P_c^{3D}$ , a central  $\text{SF}_0$  core is surrounded by a partially polarized superfluid ( $\text{SF}_P$ ) or normal phase ( $\text{N}_{\text{PP}}$ ) depending on interactions, and finally, the outer shell is  $\text{N}_{\text{FP}}$ . (b) Schematic of an array of 1D coupled tubes formed by a 2D optical lattice. By decreasing the optical lattice depth, the tunneling rate  $t$  between the tubes increases and the system crosses over from 1D to 3D.

periment employs the lowest two hyperfine sublevels of  ${}^6\text{Li}$ , the  $|F = 1/2, m_F = 1/2\rangle$  state, designated as  $|\uparrow\rangle$ , and the  $|F = 1/2, m_F = -1/2\rangle$  state, designated as  $|\downarrow\rangle$ . These correspond to the majority and the minority states, respectively. The atoms are prepared in state  $|\uparrow\rangle$ , and the population imbalance is controlled by varying the power of a single frequency sweep through the  $\sim 80$  MHz transition frequency between the  $|\uparrow\rangle$  and  $|\downarrow\rangle$  states [8]. A final step of evaporative cooling is performed in an optical trap subsequent to the creation of the spin mixture [8]. A 2D optical lattice, as depicted in Fig. 1(b), is formed by an orthogonal pair of retro-reflected laser beams at a wavelength  $\lambda$  of 1064 nm. The lattice depth  $V_L$  may be controlled up to a maximum value of

$12 E_r$  using liquid crystal retarders (LCRs) to rotate the polarization of the retro-reflected beams with respect to the incoming beams. Here,  $E_r = \hbar^2 k^2 / 2m$  is the lattice recoil energy,  $k = 2\pi/\lambda$ , and  $m$  is the atomic mass. The potential in the axial ( $z$ ) direction is approximately harmonic with a frequency  $\omega_z$  and varies linearly with  $V_L$  from  $(2\pi)197$  Hz for  $V_L = 2.5 E_r$  to  $(2\pi)256$  Hz for  $V_L = 12 E_r$ . We find that the mean number of  $|\uparrow\rangle$  atoms in the central tube,  $N_\uparrow$ , is between 160 and 240 for small ( $< 5\%$ ) polarizations, but it decreases for larger polarizations due to inefficient evaporation. The interaction strength between the two states is tuned via the wide Feshbach resonance located at 832.2 G [26, 27]. We independently control both  $t$  and the atomic interactions by varying the lattice depth and the magnetic field.

The criteria for each tube to be in the 1D regime are that both the Fermi energy  $E_F = N_\uparrow \hbar \omega_z$  and the temperature  $T$  be small compared to the transverse confinement energy:  $E_F, k_B T \ll \hbar \omega_\perp$ , where  $\omega_\perp$  is the transverse frequency within a tube. Additionally, when  $t \ll T$ ,  $E_F$  the entire bundle behaves as an array of individual 1D tubes. The value of  $E_F/\hbar \omega_\perp$  in the central tube in our experiment is between 0.2 and 0.4. Before transferring the atoms to the lattice we estimate  $T$  by fitting the *in situ* column density profiles to finite temperature Thomas-Fermi distributions and obtain  $T/T_F = 0.05$ . An upper bound for the temperature in the lattice is found by ramping the lattice on and back off with the LCRs [8]. We measure a maximum temperature of  $T/T_F = 0.16$  after this round-trip, which implies the temperature in the lattice is between these limits.

We use *in situ* phase-contrast-polarization imaging to measure the column density distributions  $n_c(x, z)$  for each spin state by two successive probe pulses, each of different near-resonant detuning from the  $^2P_{3/2}$  excited state [8, 28]. The probe pulse duration is  $\sim 5 \mu\text{s}$ , and the delay between the falling edge of the first and the rising edge of the second pulse is  $\sim 1 \mu\text{s}$ . The probe beams propagate along the  $y$ -axis, while the magnetic field and the tubes are aligned along the  $z$ -axis (see Fig. 1). We use an inverse Abel transform to obtain the full density distribution of the cloud,  $n(x, y, z)$ , from the  $n_c(x, z)$  by making use of the quasi-cylindrical symmetry about the  $z$ -axis. The number of atoms per spin state in the central tube,  $N_\uparrow$  and  $N_\downarrow$ , are extracted from the densities, and are used to calculate the central tube polarization  $P_t = (N_\uparrow - N_\downarrow)/(N_\uparrow + N_\downarrow)$ . Figures 2(a) and (b) show axial ( $z$ ) cuts of *in situ* column density images for two different magnetic fields and lattice depths for both spin states  $|\uparrow\rangle$  and  $|\downarrow\rangle$ , and for the

spin-difference,  $|\uparrow\rangle - |\downarrow\rangle$ .

It was previously shown that the axial cloud radii of the minority state distribution,  $R_\downarrow$ , and the spin difference distribution,  $R_d$ , determine the 1D-like phase boundaries [8]. These radii correspond to the axial location where the minority density and the spin difference density go to zero, respectively. Since the spin difference density is zero in the fully paired  $\text{SF}_0$  phase,  $R_d$  corresponds to the boundary between the  $\text{SF}_P$  core and the  $\text{SF}_0$  wings in 1D (Fig. 1(a)).  $R_d$  is zero for  $P_t = 0$ , but moves to larger axial radius with increasing  $P_t$  until the polarized core encompasses the entire cloud. At this polarization, which we define as  $P_c^{1D}$  [6, 8], the entire tube is in the  $\text{SF}_P$  phase and  $R_d = R_\uparrow = R_\downarrow$ . At even larger  $P_t$ , the boundary between the  $\text{SF}_P$  core and the  $\text{N}_P$  wings is defined by  $R_\downarrow$ .

The radii  $R_\downarrow$  and  $R_d$  may be extracted from the full density distributions  $n(x, y, z)$  but they may also be obtained directly from the  $n_c(x, z)$  distributions by assuming the validity of the local density approximation (LDA) in the radial direction. In this case, the chemical potential of each spin state is maximized for the central tube so that the phase boundaries,  $R_\downarrow$  and  $R_d$ , are largest for the central tube and decrease radially. We therefore use the central axial cut ( $x = 0$ ) of the  $n_c(x, z)$  distributions to locate  $R_\downarrow$  and  $R_d$ , as indicated in Fig. 2(a).

There is always a shell structure in 3D (Fig. 1(a)) and again, according to the LDA, either the density profiles or the column density profiles can be used to find the cloud radii,  $R_\downarrow$  and  $R_d$ , to locate the phase boundaries [29, 30]. At zero temperature, the center of the cloud is a balanced superfluid  $\text{SF}_0$  for  $P_t$  less than a critical polarization  $P_c^{3D}$  [31], which is the Chandrasekhar-Clogston limit in the BCS regime [32, 33]. The radius where the spin-difference density first rises above zero from the center of the cloud determines the boundary between the  $\text{SF}_0$  and the  $\text{SF}_P$  or  $\text{N}_P$  phases. Outside the partially polarized region is a  $\text{N}_P$  shell, whose boundary is defined by  $R_\downarrow$ . Atoms in the  $\text{N}_P$  shell are non-interacting, so the outer boundary of the cloud is  $R_\uparrow$  which is also equivalent to  $R_d$  here.

Figure 2(a) shows a 1D-like profile, where the spin-difference column density profile is approximately parabolic, in contrast to Fig. 2(b) where the nearly flat-topped profile indicates a central  $\text{SF}_0$  phase that is consistent with 3D phase separation [2, 34]. The distinction between 3D and 1D phase separation is confirmed by examination of the local polarization  $p(0, 0, z)$  at the center of the cloud  $p_0 = p(0, 0, 0)$  obtained from the inverse Abel transformed data. In Fig. 2(c),  $p_0$  is greater than zero,

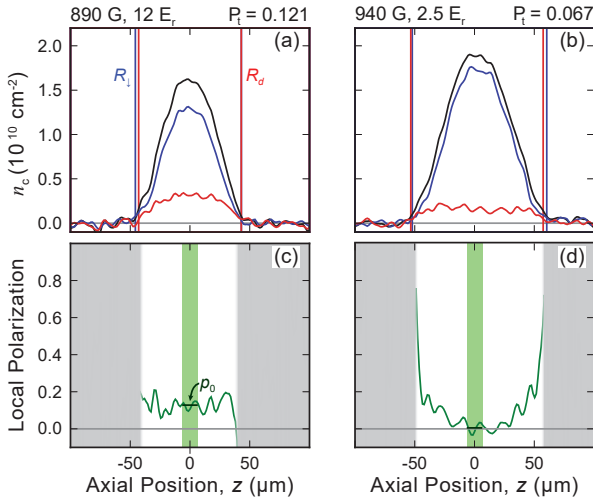


FIG. 2. (Color online) (a, b) Column density profiles and (c, d) the corresponding local polarization  $p(0, 0, z)$  profiles of spin-imbalanced gases. These profiles are smoothed using a Gaussian function with width of 4 pixels, where 1 pixel =  $1.33 \mu\text{m}$ . The values of magnetic field, lattice depth, and the central tube polarization  $P_t$  are indicated above each column. (a) and (b) The  $|\uparrow\rangle$ ,  $|\downarrow\rangle$ , and their difference are indicated by the black, blue and red curves, respectively.  $R_d$  and  $R_d$  are indicated by the red and blue vertical lines. (c) and (d) Local polarization found from the difference between the majority and minority density profiles along the central tube using a weighted average of the central 7 tubes. The green band shows the  $13 \mu\text{m}$  region along  $z$  that is used to average the local polarization to find  $p_0$ . The grayed out regions are where  $N_\downarrow$  is consistent with the background noise and thus, where the local polarization is poorly defined. The entire cloud in (a) and (c) is SF<sub>P</sub>, while in (b, d), there is an extended region of SF<sub>0</sub> in the center of the cloud ( $p_0 = 0$ ), then a region of SF<sub>P</sub> or N<sub>PP</sub>.

implying a partially polarized phase consistent with 1D phase separation, while Fig. 2(d) shows an example with  $p_0 = 0$  and is therefore a 3D phase separation containing an SF<sub>0</sub> core.

Two examples of phase diagrams constructed from the radii  $R_d$  and  $R_d$  are presented in Figs. 3(a) and (b). Figure 3(a) corresponds to a relatively deep lattice, with  $V_L = 12 E_r$ , that exhibits a 1D-like phase diagram for which the core is polarized. The distinguishing characteristics of the 1D-like phase diagram are 1)  $R_d$  crosses  $R_d$  at a non-zero  $P_c^{1D}$ , and 2)  $R_d$  goes to zero as  $P_t$  goes to zero. Figure 3(b) shows an example of a 3D-like phase diagram where the centrally located phase is SF<sub>0</sub>. In a strictly 3D system,  $R_d$  decreases with decreasing  $P_t$  until meeting  $R_d$  at  $P_t = 0$ . In this quasi-3D system, however,  $R_d$  is seen to cross  $R_d$  at non-zero  $P_t$ , corresponding to

a small, but non-zero  $P_c^{1D}$ .

Phase separation in 3D is distinguished by the presence of a superfluid core that is suppressed at a critical polarization  $P_c^{3D}$  [13–15]. The core radius may be identified by locating the polarization where  $R_d$  first rises above zero from the center of the cloud. Due to the noise in the inverse Abel transformed data, however, we instead find  $P_c^{3D}$  by measuring  $p_0$ , which we find to be less sensitive to noise.  $P_c^{3D}$  is the central tube polarization  $P_t$ , above which  $p_0$  begins to rise from zero. For  $P_c^{3D} = 0$ , there is no balanced core for any  $P_t$ , and thus the gas is 1D-like. Figure 3(c) shows  $p_0$  corresponding to the 1D phase diagram of Fig. 3(a). In this case,  $p_0$  increases linearly with  $P_t$ . By decreasing  $V_L$  sufficiently, a kink appears in  $p_0$ , as shown in Fig. 3(d), where the intercept gives  $P_c^{3D}$ . The insets of Fig. 3 show the fitted portion of  $p_0$  versus  $P_t$  in detail.

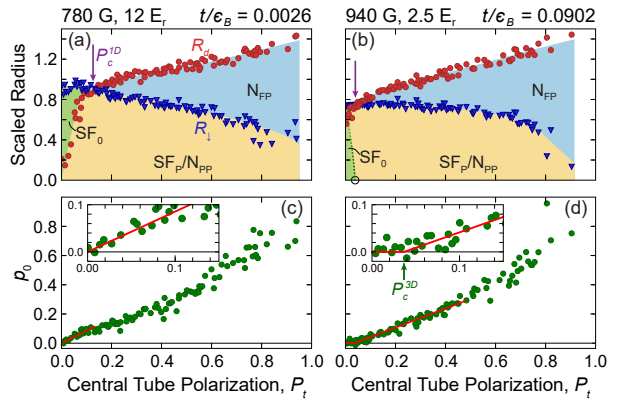


FIG. 3. (Color online) (a) 1D- and (b) 3D-like phase diagrams.  $R_d$  ( $\blacktriangledown$ ) and  $R_d$  ( $\bullet$ ) are scaled by  $N^{1/2}l_z$  [6, 8], where  $l_z = \sqrt{\hbar/m\omega_z}$  is the axial harmonic oscillator length and  $N = N_\uparrow + N_\downarrow$ . The colored regions correspond to the indicated phases, as defined in Fig. 1. The boundaries between the phases follow the data. In (b), the open circle indicates the measured  $P_c^{3D}$  from (d). The dotted line is an extrapolation from  $P_c^{3D}$ . (c) and (d) The local central polarization  $p_0$  vs.  $P_t$ , used to find  $P_c^{3D}$ . The insets show the central region near  $P_c^{3D}$ . The solid red line is a fit to the data to find  $P_c^{3D}$ , using a function with a bilinear slope [15]. The vertical arrows indicate  $P_c^{1D}$  (purple) and  $P_c^{3D}$  (green). The gas becomes more 3D-like as  $P_c^{1D}$  decreases and  $P_c^{3D}$  increases. Each data point is the average of  $\sim 10$  experimental realizations, binned with width  $\Delta P_t = 0.005$ .

Figures 4(a) and (b) show  $P_c^{1D}$  and  $P_c^{3D}$  for several interaction strengths. We calculate  $t$  from the eigenenergies of the 1D Hamiltonian [35] which includes nearest neighbor and next-nearest neighbor contributions. The next-nearest neighbor term begins to contribute at lattice depths below  $5 E_r$ . Fig-

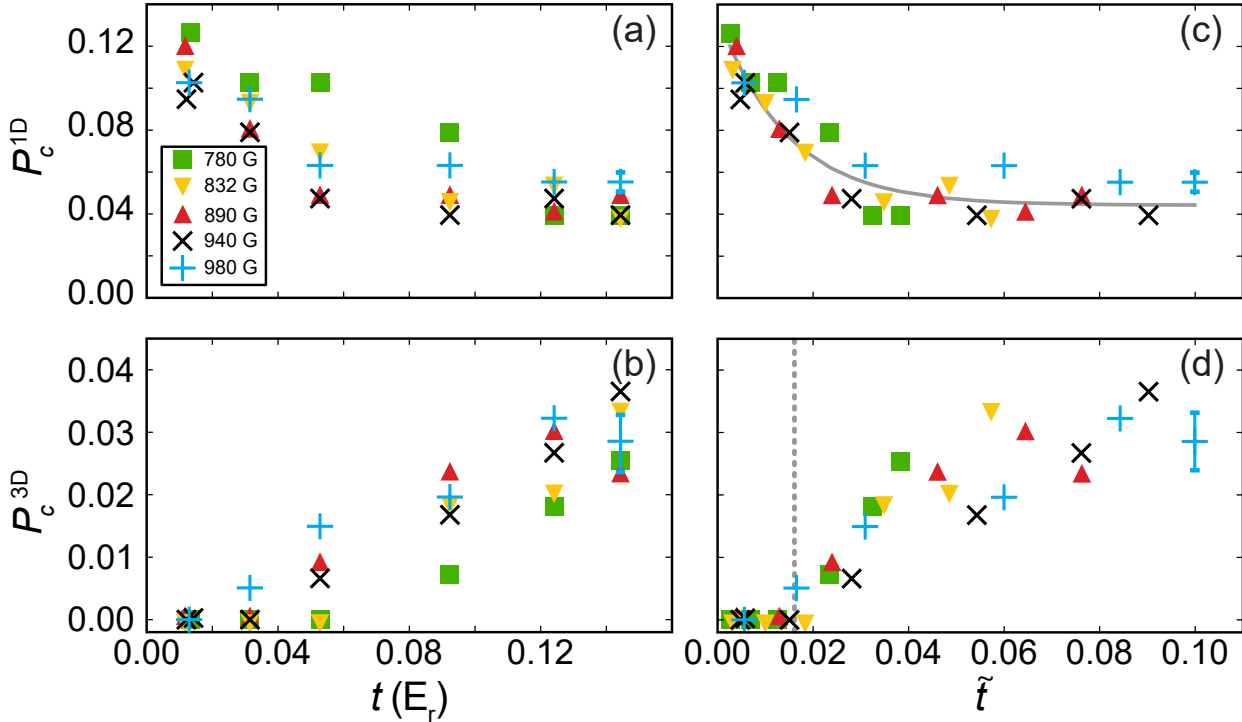


FIG. 4. (Color online) (a)  $P_c^{1D}$  and (b)  $P_c^{3D}$  vs.  $t$ . Ordered from lowest to highest field, the corresponding  $a_{3D}$  are:  $6170 a_0$ , unitarity,  $-8610 a_0$ ,  $-5360 a_0$ , and  $-4340 a_0$ , in units of the Bohr radius  $a_0$ . The corresponding ranges of  $\epsilon_B$  depending on lattice strength are:  $3.8 - 5.2 E_r$ ,  $2.5 - 3.7 E_r$ ,  $1.9 - 2.9 E_r$ ,  $1.6 - 2.5 E_r$ , and  $1.4 - 2.3 E_r$ , respectively. (c)  $P_c^{1D}$  and (d)  $P_c^{3D}$  versus the scaled tunneling rate  $\tilde{t} = t/\epsilon_B$ . The critical polarizations collapse onto a single curve when plotted against the scaled tunneling  $\tilde{t}$ . The 1D to 3D crossover is indicated by the dotted line in (d), where  $\tilde{t}_c = 0.016(1)$ , the value above which the gas has an  $SF_0$  core. Fitting  $P_c^{1D}$  in (b) to an exponential gives a  $1/e$  decay of  $\tilde{t} = 0.015(1)$ . The uncertainty in  $P_t$  is estimated from 10 images known to be balanced.

ures 4(a) and (b) show that the 3D regime is attained for larger  $t$ , as expected, but also for larger magnetic field, corresponding to weaker attractive interactions, and thus larger chemical potentials.

In Figs. 4(c) and (d), we replot the data against the scaled tunneling rate  $\tilde{t} = t/\epsilon_B$ , where  $\epsilon_B$  is the pair binding energy, calculated from [36]

$$\frac{\sqrt{2}l_\perp}{a_{3D}} = -\zeta \left[ \frac{1}{2}, \frac{-\epsilon_B}{2\hbar\omega_\perp} \right], \quad (1)$$

and where  $\zeta$  is the Hurwitz zeta function. This solution depends on the lattice frequency  $\omega_\perp$ , the transverse harmonic oscillator length  $l_\perp = \sqrt{\hbar/m\omega_\perp}$ , as well as the 3D s-wave scattering length  $a_{3D}$ . When scaled in this way the data collapse onto a single curve, thus demonstrating the universality of the crossover [9]. By fitting the data of Fig. 4(d) with  $\tilde{t} < 0.04$  to a bilinear function, we find the intercept to be  $\tilde{t}_c = 0.016(1)$ . The uncertainty is the combination from the standard error of the fit and the uncertainty in the measurements of  $V_L$  and the magnetic

field. All clouds with  $\tilde{t} > \tilde{t}_c$  possess a superfluid core, which is a 3D-like characteristic. As seen in Fig. 4(c),  $P_c^{1D}$  decreases exponentially with a decay constant of  $\tilde{t} = 0.015(1)$ , where the uncertainty has the same origins. This suppression of  $P_c^{1D}$  is quantitatively consistent with the onset of 3D behavior and provides a confirming measure of  $\tilde{t}_c$ .

A mean field analysis predicts that the phase boundary between the  $SF_0$  core and the NFP phase corresponds to a first order transition [9]. Due to noise in the density profiles from the inverse-Abel transformed data, however, we are unable to directly observe a jump in the local polarization. This could also be a consequence of finite  $T$ . Finally, the mean-field analysis also predicts that the 3D to 1D crossover may be driven by increasing the chemical potential  $\mu$  [9]. The slope of this boundary, however, is very steep in the  $\mu$  vs.  $h$  plane, where  $h$  is the chemical potential difference. Since our measurements are performed in the regime where  $P_t \rightarrow 0$ , or equivalently  $h \rightarrow 0$ , a possible  $\mu$ -dependent transition could only occur at very large  $\mu$  where the 1D

criterion for each tube no longer holds.

Our results show that the 1D to 3D crossover occurs at a universal scaled tunneling,  $\tilde{t}_c = 0.016(1)$ . The crossover region is predicted to be the most robust against fluctuations in FFLO wavenumber and temperature [9], suggesting the most fruitful parameter region to search for the FFLO phase is the quasi-1D regime near  $\tilde{t}_c$ .

The authors would like to thank Erich Mueller, Dan Sheehy and David Huse for many valuable discussions. This work was supported by grants from the NSF, ONR, the Welch Foundation, and the ARO-MURI program.

---

\* Current address: AOSense Inc., Sunnyvale, CA 94085

- [1] S. Giorgini, L. P. Pitaevskii, and S. Stringari, *Rev. Mod. Phys.* **80**, 1215 (2008).
- [2] L. Radzihovsky and D. E. Sheehy, *Rep. Prog. Phys.* **73**, 076501 (2010).
- [3] I. Bloch, J. Dalibard, and W. Zwerger, *Rev. Mod. Phys.* **80**, 885 (2008).
- [4] P. Fulde and R. A. Ferrell, *Phys. Rev.* **135**, A550 (1964).
- [5] A. I. Larkin and Y. N. Ovchinnikov, *JETP* **47**, 1136 (1964).
- [6] G. Orso, *Phys. Rev. Lett.* **98**, 070402 (2007).
- [7] H. Hu, X.-J. Liu, and P. Drummond, *Phys. Rev. Lett.* **98**, 070403 (2007).
- [8] Y. A. Liao, A. S. C. Rittner, T. Paprotta, W. Li, G. B. Partridge, R. G. Hulet, S. K. Baur, and E. J. Mueller, *Nature* **467**, 567 (2010).
- [9] M. M. Parish, S. K. Baur, E. J. Mueller, and D. A. Huse, *Phys. Rev. Lett.* **99**, 250403 (2007).
- [10] E. Zhao and W. V. Liu, *Phys. Rev. A* **78**, 063605 (2008).
- [11] K. Sun and C. J. Bolech, *Phys. Rev. A* **87**, 053622 (2013).
- [12] M. O. J. Heikkilä, D.-H. Kim, M. Troyer, and P. Törmä, *Phys. Rev. Lett.* **113**, 185301 (2014).
- [13] G. B. Partridge, W. Li, R. I. Kamar, Y. A. Liao, and R. G. Hulet, *Science* **311**, 503 (2006).
- [14] Y. Shin, M. W. Zwierlein, C. H. Schunck, A. Schirotzek, and W. Ketterle, *Phys. Rev. Lett.* **97**, 030401 (2006).
- [15] B. A. Olsen, M. C. Revelle, J. A. Fry, D. E. Sheehy, and R. G. Hulet, *Phys. Rev. A* **92**, 063616 (2015).
- [16] C. Castellani, C. D. Castro, and W. Metzner, *Phys. Rev. Lett.* **72**, 316 (1994).
- [17] A. Görlitz, J. M. Vogels, A. E. Leanhardt, C. Raman, T. L. Gustavson, J. R. Abo-Shaeer, A. P. Chikkatur, S. Gupta, S. Inouye, T. Rosenband, and W. Ketterle, *Phys. Rev. Lett.* **87**, 130402 (2001).
- [18] G. E. Astrakharchik and S. Giorgini, *Phys. Rev. A* **66**, 053614 (2002).
- [19] F. Gerbier, *Europhys. Lett.* **66**, 771 (2004).
- [20] J. Armijo, T. Jacqmin, K. Kheruntsyan, and I. Bouchoule, *Phys. Rev. A* **83**, 021605(R) (2011).
- [21] M. M. Calbi, S. M. Gatica, and M. W. Cole, *Phys. Rev. B* **67**, 205417 (2003).
- [22] E. W. Carlson, D. Orgad, S. A. Kivelson, and V. J. Emery, *Phys. Rev. B* **62**, 3422 (2000).
- [23] B. Pan, Y. Wang, L. Zhang, and S. Li, *Inorg. Chem.* **53**, 3606 (2014).
- [24] H. Moritz, T. Stöferle, K. Günter, M. Köhl, and T. Esslinger, *Phys. Rev. Lett.* **94**, 210401 (2005).
- [25] A. Vogler, R. Labouvie, G. Barontini, S. Eggert, V. Guarnera, and H. Ott, *Phys. Rev. Lett.* **113**, 215301 (2014).
- [26] M. Houbiers, H. T. C. Stoof, W. I. McAlexander, and R. G. Hulet, *Phys. Rev. A* **57**, R1497(R) (1998).
- [27] G. Zürn, T. Lompe, A. N. Wenz, S. Jochim, P. Julienne, and J. M. Hutson, *Phys. Rev. Lett.* **110**, 135301 (2013).
- [28] C. C. Bradley, C. A. Sackett, and R. G. Hulet, *Phys. Rev. Lett.* **78**, 985 (1997).
- [29] G. Bertaina and S. Giorgini, *Phys. Rev. A* **79**, 013616 (2009).
- [30] Y. Shin, A. Schirotzek, C. H. Schunck, and W. Ketterle, *Phys. Rev. Lett.* **101**, 070404 (2008).
- [31] Since  $P_c^{3D}$  is defined with respect to the central tube polarization, not the global cloud polarization, there is an offset in the polarization between our  $P_c^{3D}$  and previous determinations.
- [32] B. S. Chandrasekhar, *Appl. Phys. Lett.* **1**, 7 (1962).
- [33] A. M. Clogston, *Phys. Rev. Lett.* **9**, 266 (1962).
- [34] Y. Shin, C. H. Schunck, A. Schirotzek, and W. Ketterle, *Nature* **451**, 689 (2008).
- [35] O. Morsch and M. Oberthaler, *Rev. Mod. Phys.* **78**, 179 (2006).
- [36] T. Bergeman, M. G. Moore, and M. Olshanii, *Phys. Rev. Lett.* **91**, 163201 (2003).